Enhanced thermal stability and mechanical properties of high-temperature resistant Al−Cu alloy with Zr and Mn micro-alloying

Teng-teng SUN[1,2], Ji-wei GENG[1,2], Ze-yu BIAN[1,2], Yi WU[1,2],
Ming-liang WANG[1], Dong CHEN[2,3], Nai-heng MA[2], Hao-wei WANG[1,2]

1. School of Materials Science and Engineering, Shanghai Jiao Tong University, Shanghai 200240, China;
2. State Key Laboratory of Metal Matrix Composites, Shanghai Jiao Tong University, Shanghai 200240, China;
3. Anhui Aluminum Matrix Composites Engineering Research Centre, Huaibei 235099, China

Abstract: The high temperature (HT) thermal stability and mechanical properties of Al−5%Cu (AC) and Al−5%Cu−0.2%Mn−0.2Zr% (ACMZ) alloys from 573 to 673 K were systematically studied. The results displayed that micro-alloying additions of Zr and Mn elements have presented a significant role in stabilizing the main strengthening metastable θ' precipitates at a temperature as high as 573 K. Simultaneously, the HT tensile test demonstrated that ACMZ alloy retained their strength of (88.6±8.8) MPa, which was much higher than that of AC alloy ((32.5±0.8) MPa) after the thermal exposure at 573 K for 200 h. Finally, the underlying mechanisms of strength and ductility enhancement mechanism of the ACMZ alloy at HT were discussed in detail.
Key words: Al−Cu alloy; micro-alloying; thermal stability; precipitate evolution; high-temperature mechanical properties

1 Introduction

Nowadays, automotive engines are moving toward higher power density designs to meet stringent fuel economy standards. For example, the peak temperatures for cylinder heads are projected to increase from ~503 K in current engines to over 573 K in the future [1,2]. Thus, it is required for alloys to possess relatively good high temperature (HT) stability used for engine components. Al alloys that contain Al-based precipitates are potential candidates for structural applications at both room temperature (RT) and HT because of their significantly lower density and higher specific strength [3−5]. However, the current widely used Al alloys, like Al−Zn−Mg [6], Al−Mg−Si [7], and Al−Cu [8] alloys show poor

stability and mechanical properties at 573 K. Herein, the Al−Cu alloy is the typical Al alloy applied at HTs in the automotive, military, and aerospace industries. Indeed, this alloy can hardly meet the increasing standards of structural stability and mechanical properties under severe service conditions [9]. Therefore, multiple efforts to improve the HT mechanical properties of the Al−Cu alloy are still required [10,11].

For binary Al−Cu alloys, the biggest detriment factor to the HT mechanical properties is possibly the coarsening and subsequent transformation of their strengthening precipitates. The precipitation sequence in Al−Cu alloys is as follows: supersaturated solid solution → Guinier−Preston zones (GP-I zones) → θ'' (GP-II zones) → plate-shaped θ' → rod-shaped or globular incoherent θ [12], where θ'' and θ' are the main precipitation-

strengthening phases in Al−Cu alloys [13].

In recent years, micro-alloying has become an effective strategy to strengthen the Al alloys [14−16]. Normally, there are high densities of nano-size precipitates with the addition of micro-alloying elements, which significantly strengthen Al alloys. Adding elements such as Mg, Mn, Li, Sn, and RE (rare elements) into Al−Cu alloys can adjust Al_2Cu nucleation and growth by affecting nucleation kinetics, volumetric misfit strain, shear strain, and interfacial energy of θ' phases [17]. SHIN et al [18] used first-principles calculation to show that the co-addition of Mn and Zr elements into Al−Cu alloy can effectively improve the HT stability of the alloy. The reason is that Mn has segregated on the coherent wide surface of the θ' phase, and Zr has segregated on the rim of semi-coherent, thereby inhibiting the coarsening and growing behavior of θ' precipitates at HTs. Apart from HT stability, both strength and ductility are also essential requirements during industrial application. Since Al−Cu alloys are widely used in the automotive field, it is of imperative importance to study the properties which should be considered for design phase of automotive structures. Thus, studying the HT mechanical properties (i.e., yield strength and tensile ductility) which are often correlated with fracture toughness is important. Nevertheless, SHYAM et al [19] did not elaborate on the mechanical properties such as tensile strength at both RT and HT for the Al−Cu alloy. Hence, we investigated the effect of micro-alloying with Mn and Zr on the precipitation and coarsening behaviors of the θ' phase and the mechanical performance at both RT and HT of the Al−Cu alloy in this study. The underlying mechanisms of strength and ductility enhancement of the Al−Cu-based alloys at HT were discussed in detail.

2 Experimental

2.1 Alloy casting and heat treatments

Two types of alloys (i.e., the Al−5wt.%Cu (AC) alloy and the AC alloy with 0.2wt.%Mn−0.2wt.%Zr additions (ACMZ)) were melted in a clean iron crucible, respectively. The crucible was coated with boron nitride paint. To cast the alloys, the pure Al and binary alloys of Al−50wt.%Cu, Al−10wt.%Mn, and Al−10wt.%Zr were used in this experiment.

Placing the crucible inside an electric resistance furnace, the melting process was carried out. At the beginning, the raw materials were heated up to 1033 K to form the melt. Afterwards, the melt temperature was increased to 1123 K and held for 30 min. This procedure can ensure that all alloy elements were completely dissolved in the melt. Then, the melt temperature decreased back to 1033 K, followed by the melt purification using the refining agent. Subsequently, a vacuum furnace was used to degas melt at 1033 K for 10 min. Finally, the melt was poured into a preheated cast iron mold at ~1013 K. The composition measurements of both as-cast alloys were performed by the inductively coupled plasma-atomic emission spectrometry (ICP-AES, iCAP7600), and the results were shown in Table 1. The nominal compositions of both as-cast alloys are in good agreement with the ICP results, suggesting that the casting control for both alloys was successful.

Table 1 Compositions of as-cast Al alloys (wt.%)

Alloy	Nominal composition			
	Cu	Mn	Zr	Al
AC	5.0	−	−	Bal.
ACMZ	5.0	0.2	0.2	Bal.

Alloy	ICP results					
	Cu	Mn	Zr	Fe	Si	Al
AC	5.3	−	−	0.01	<0.01	Bal.
ACMZ	5.2	0.21	0.15	0.02	<0.01	Bal.

The cast ingots were subjected to heat treatments thereby. In this case, both ingots were solution-treated at 803 K for 5 h, and quenched into RT water immediately, and finally aged at 463 K for 0−28 h.

2.2 Microstructure analysis

The phase compositions were detected by X-ray diffraction (XRD, D8 ADVANCE Da Vinci) from 2θ values from 20° to 90° at a speed of 2 (°)/min. The optical microscope (OM) was used to observe metallographic structure. Polarized light was used to obtain the grain size for both alloys. The scanning electron microscope (SEM, TESCAN MAIA3) was applied to characterizing the alloy microstructure. The energy dispersive spectroscope (EDS) was equipped on the SEM to make the

compositional analysis. The observed surfaces were metallurgically polished up to 0.5 μm diamond paste and etched using Keller's solution (1.5 vol.% HCl + 2.5 vol.% HNO$_3$ + 1 vol.% HF + 95 vol.% deionized water) by 10 s immersion. The micro-structure details and phase identification were obtained using a transmission electron microscope (TEM, JEM−2100). The TEM samples were prepared by mechanical polishing up to 80 μm. Thin foils were produced by twin-jet electro-polishing method using 30% nitric acid solution in methanol at 243 K. Thin Al grains were chosen so that they could be oriented precisely via a double-tilt specimen holder in the $\langle 100 \rangle_{Al}$ zone axis direction to allow θ'/θ''-Al$_2$Cu precipitates to be viewed edge-on in two habit planes. Precipitation behaviors of θ'' and θ' precipitates were assessed directly by bright field (BF) and dark field (DF) TEM measurement.

2.3 Mechanical testing

The Vickers hardness (HV) tests for both alloys were carried out using Vickers indentation (EZ-mat, CARAT 930) at 5 kg load and RT. Indentation surfaces were metallurgically polished up to 2500 grit SiC paper, and the indenter was kept in contact with the specimen surface for 10 s. Eight indentations were performed on the circular section of a cylinder with a diameter of 10 mm. The average hardness value was calculated, and the error bars were standard deviations around the mean values of hardness.

Tensile tests were carried out on a Zwick/Roell machine at a fixed crosshead velocity of 5×10^{-4} m/s. These test samples were processed into a dog-bone-like shape according to ASTM standard B557M─84. For the as-aged alloys, tensile tests were directly performed at RT after peak-aged treatment. The HT (573 K) tensile tests of both alloys with or without prior stabilization for 200 h at 573 K were performed. At least, three samples were tested for each case, and all the repeated test

curves showed similar behavior. The fractured samples were air-cooled following the testing.

2.4 Thermal stability testing

The HT stability of the samples was tested through the thermal exposure experiment up to 200 h. The thermal exposure test of both alloys was performed in the furnace (Nabertherm N60/85HA) at the peak-aged state. Overall, the experimental conditions for both alloys were provided in Table 2.

3 Results

3.1 Cast alloy microstructure

Figure 1 shows the typical optical micrographs and corresponding magnified SEM images for both as-cast alloys. A large number of solutes are segregated to grain and sub-GBs caused under non-equilibrium cooling conditions. The average secondary arm spacing is ~26 μm for AC alloy, and ~27 μm for ACMZ alloy. For the as-cast AC alloy (Fig. 1(a)), the Al−Al$_2$Cu(θ) eutectic exhibits network morphology at GBs, which can be eliminated by the further heat-treatment process.

In comparison, the as-cast ACMZ alloy shows that there are more eutectic Al$_2$Cu(θ) phases in the matrix (as indicated by the arrow in Fig. 1(c)), and such phases show strip shape with the mesh structure. According to EDS analysis (Table 3), the eutectic phases at GBs for both as-cast alloys are confirmed to be Al$_2$Cu(θ) phases, mainly consisting of Al and Cu with the Al/Cu molar ratio of approximately 2:1. Clearly, both Mn and Zr elements are not identified on GBs, indicating that these alloying elements should remain in the matrix. This is consistent with the XRD analysis shown in Fig. 2.

3.2 Aging response and microstructure

Figure 3 shows the aging behaviors for both alloys at 463 K. In detail, both alloys exhibit the obvious age-hardening behavior. For AC alloy, the

Table 2 Summary of heat treatments performed on Al alloys

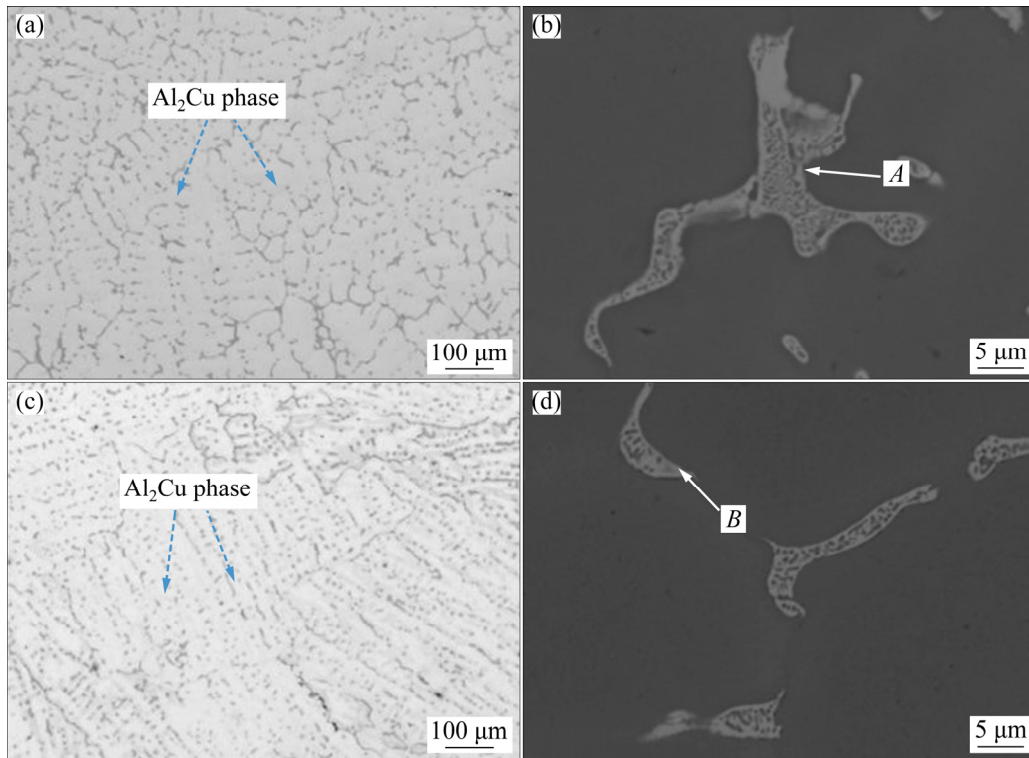| Alloy	Solution treatment	Aging treatment	Thermal exposure treatment
AC	803 K, 5 h	463 K, peak aging	573 K@Exposure(0−200 h) 623 K@Exposure(0−200 h)
ACMZ	803 K, 5 h	463 K, peak aging	573 K@Exposure(0−200 h) 623 K@Exposure(0−200 h) 673 K@Exposure(0−200 h)

Fig. 1 OM images of as-cast AC (a, b) and ACMZ (c, d) alloys

Table 3 EDS results for Points *A* (Fig. 1(b)) and *B* (Fig. 1(d)) (at.%)

Point	Al	Cu
A	67.8	32.2
B	64.4	35.6

Fig. 2 XRD patterns of samples
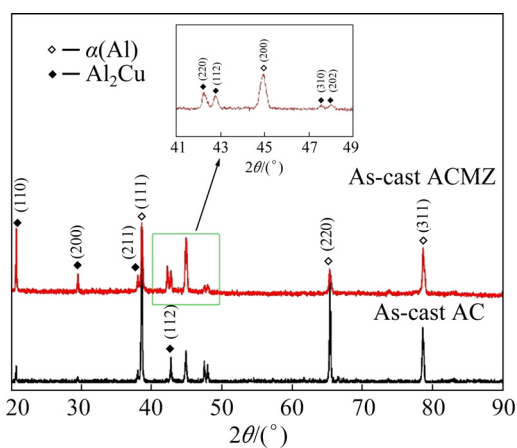

Fig. 3 Vickers hardness of AC and ACMZ alloys aged at 463 K for different time

aging process is divided into three stages: under-aging (UA), peak-aging (PA), and over-aging (OA) states. The AC alloy shows a rapid hardening response and reaches the PA state at 4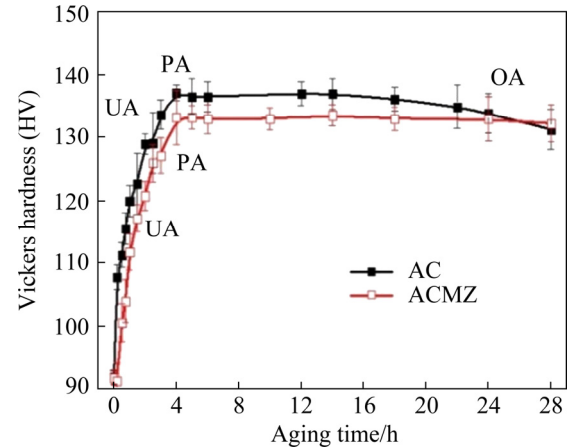 h aging treatment. At the OA state, the PA hardness value can maintain nearly unchanged from 4 to 18 h. Finally, there is an obvious softening behavior at 0.5 HV/h from 18 to 28 h in the AC alloy. In comparison, the ACMZ alloy has similar age-hardening behavior with the AC alloy, which also uses 4 h to reach the PA state. Notably, the ACMZ shows a bit lower PA hardness value than the AC alloy. Nevertheless, the ACMZ alloy is more stable in the OA state and has rarely hardness reduction from 4 to 28 h. At the 28 h aging treatment, the ACMZ alloy has an even higher hardness than the

AC alloy. As a result, it can be inferred that with the additions of Mn and Zr into Al−Cu-based alloy, the precipitation behavior may hardly change, but the thermal stability of the precipitate phase is probably enhanced in the ACMZ alloy.

Figure 4 shows the polarized optical microstructure and the corresponding SEM images to show the magnified microstructure of these as-PAed alloys. Normally, the AC alloy has an average grain size of ~250 μm (Fig. 4(a)), and the ACMZ alloy has an average grain size of ~223 μm (Fig. 4(c)). Therefore, both alloys show the comparably coarse grain size to indicate the limited grain strengthening effect. Furthermore, the element maps show that there are still Al$_2$Cu(θ) phases in both alloys to a fewer extent (Figs. 4(b) and (d)).

3.3 RT mechanical properties

Tensile tests were carried out on both alloys, and ultimate tensile strength (UTS), yield strength (YS), and elongation (EL) to failure were obtained. Figure 5(a) shows RT tensile engineering stress−strain curves of both AC and ACMZ alloys at the PA state. Both alloys show little or no load drop before fracture, indicating no sample scale necking during tensile testing. The samples have fractured in a region of homogeneous deformation, and the corresponding YS, UTS, and EL to failure are summarized in Fig. 5(b). In detail, the values of YS, UTS, and EL are (291±12.6) MPa, (401±0.7) MPa, and (10.5±0.2)% for AC alloy, and

(292.5±15.8) MPa, (403.9±5.6) MPa, and (11.9±1.2)% for ACMZ alloy. Besides, Figures 5(c) and (d) show the fracture morphologies of both alloys. In detail, they are composed of rock candy and cleavage patterns, indicating the intergranular fracture in both alloys [20].

3.4 HT properties

3.4.1 HT stability

To estimate the HT stability, thermal exposure experiments have referred to placing the as-PAed alloys at HTs up to 200 h. Figure 6(a) displays the dependence of hardness values for AC and ACMZ alloys on the holding duration at 573 and 623 K.

For the 573 K@Exposure(0−200 h) condition, the AC alloy shows a three-stage hardness reduction behavior, including: (1) 0−2 h, the hardness declines at a higher rate of 19.1 HV/h; (2) 2−24 h, the alloy hardness is stabilized with a smaller softening rate of 0.4 HV/h; (3) 24−200 h, the alloy is softened at a rate of 0.1 HV/h, possibly suggesting the coarsening of the precipitates. For the ACMZ alloy, there is a two-stage thermal exposure response showing in the hardness curve as follows: (1) 0−2 h, the hardness declines at a higher rate of 19.1 HV/h, and this stage is similar to the AC alloy; (2) 2−200 h, the hardness is merely changed, suggesting the stability of the precipitates. Comparably, the ACMZ alloy has a much better thermal stability under 573 K@Exposure(0−200 h) condition. Although both the alloys have similar
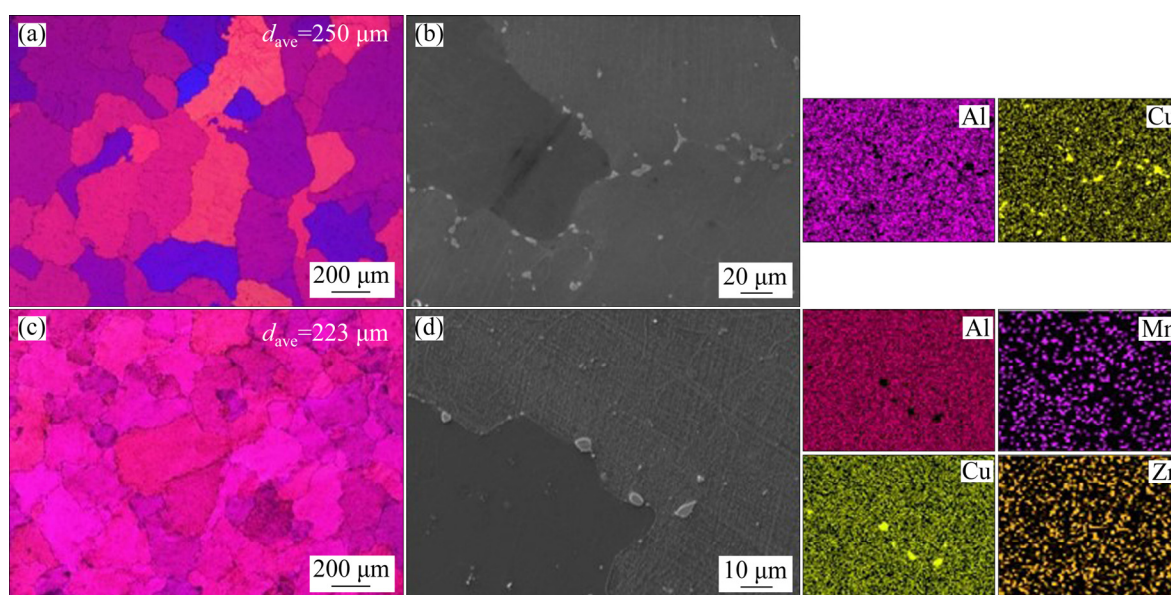

Fig. 4 Polarized light optical micrographs of AC (a, b) and ACMZ (c, d) alloys at PA states (The corresponding composition mappings of Al, Cu, Mn and Zr are shown on the right, respectively)
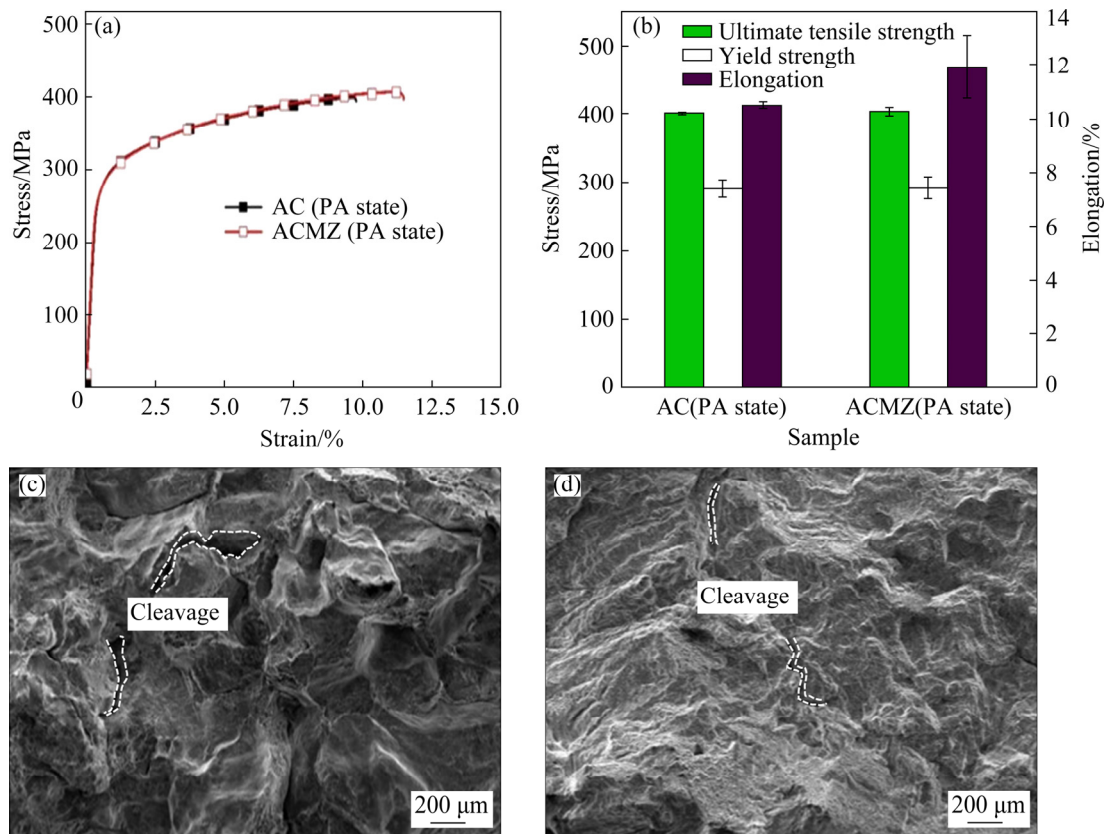
Fig. 5 Tensile stress−strain curves at RT (a), UTS, YS and EL for AC and ACMZ alloys (b), and tensile fractured morphologies of AC (c) and ACMZ (d) alloys
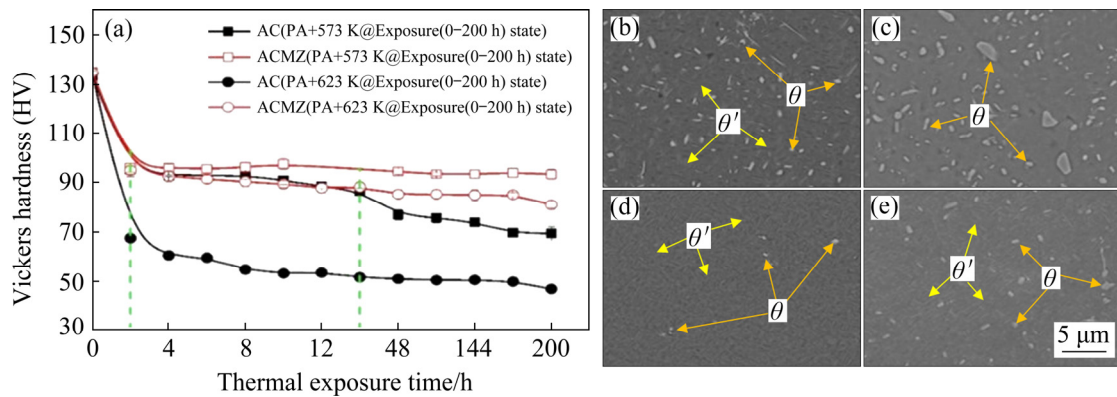

Fig. 6 Hardness values for as-PAed AC and ACMZ alloys (a), SEM images of AC (b) and ACMZ (d) alloys at 573 K@Exposure(200 h) state, and AC (c) and ACMZ (e) alloys at 623 K@Exposure(200 h) state

hardness values at the beginning, the hardness of the ACMZ alloy remains at ~95 HV, which is ~20 HV higher than that of the AC alloy (~75 HV) at the end of thermal exposure.

For the 623 K@Exposure(0−200 h) condition, the AC alloy shows a two-stage hardness reduction behavior, including: (1) 0−2 h, the hardness declines at a much higher rate of 33.5 HV/h; (2) 2−200 h, the alloy hardness is stabilized with a softening rate of 0.3 HV/h. For the ACMZ alloy in

the 623 K@Exposure(0−200 h) condition, there is also a two-stage thermal exposure response showing in the hardness curve as follows: (1) 0−2 h: the hardness declines at a rate of 22.1 HV/h, which is smaller than the AC alloy; (2) 2−200 h, the alloy hardness is stabilized with a smaller softening rate of 0.1 HV/h. At the end of the 623 K@-Exposure(200 h) state, the hardness retention ratio of AC alloy is only 35% with hardness of ~47 HV, which is lower than its as-cast hardness of ~59 HV.

This has indicated that the AC alloy has completely lost its precipitation strengthening effect in this condition. For ACMZ alloy, the value of retention ratio is 60% with a much higher hardness of ~81 HV, still higher than its as-cast hardness of ~63 HV.

The microstructure variations for both alloys were studied by SEM at 573 K@Exposure(200 h) and 623 K@Exposure(200 h) states (Figs. 6(b−e)). Herein, some obvious differences can be identified. For AC alloy at 573 K@Exposure(200 h) state (Fig. 6(b)), there are major plate-shaped (Length: 0.94 μm) and some cubic-shaped (Length: 0.65 μm; Width: 0.44 μm) particles widely distributed in the Al matrix, indicating that the precipitation strengthening effect has been weakened by the appearance of larger particles. Furthermore, at 623 K@Exposure(200 h) state (Fig. 6(c)), the precipitates shape has completely changed from plate to a larger bulk morphology, and these particles are irregularly distributed in the Al matrix.

For ACMZ alloy, the microstructures are completely composed of plate-shaped precipitate (Length: 0.8 μm) at 573 K@Exposure(200 h) state (Fig. 6(d)). Even at 623 K@Exposure(200 h) state (Fig. 6(e)), there are major plated-shape precipitates with few smaller bulk particles. This observation has suggested that both Mn and Zr elements can greatly improve the HT microstructure stability of Al−Cu alloy after the extended exposure at a temperature up to 623 K.

3.4.2 HT mechanical properties

The HT tensile test was carried out at 573 K. Before the tensile test, each tensile bar mounted for testing was kept in the test chamber for 30 min at 573 K to stabilize the sample. Figure 7(a) shows the representative engineering stress−strain tensile curves for AC and ACMZ alloys. Tensile curves display a huge difference for both alloys with or without the 573 K@Exposure(200 h) treatment.

For AC alloy, compared with the as-PAed tensile state, the tensile strength decreases significantly at the PA+573 K@Exposure(200 h) state. The UTS and YS decrease from (80.7±0.7) and (69.8±1.2) MPa to (34.2±1.8) and (32.5±0.8) MPa, respectively. But the EL increases from (14.1±0.1)% to (39.7±1.0)%, indicating that HT softening of AC alloy occurs under this condition. The ACMZ alloy displays a comparatively slight change in both conditions. The UTS and YS change from (117.5±3.2) and (99.84±0.3) MPa at PA state to (124.9±5.8) and (88.6±8.8) MPa at the PA+573 K@ Exposure(200 h) tensile state. At the same time, EL increases from (8.5±0.5)% to (18.3±3.3)%, indicating that both Mn and Zr additions to AC alloys can greatly improve the HT strength with improved ductility (Fig. 7(b)).

The effects of the work hardening rate (WHR, $d\sigma/d\varepsilon$) on the true strain (ε) and $\sigma−\sigma_y$ are given for AC (Fig. 7(c)) and ACMZ (Fig. 7(d)) alloys. For AC alloy, the WHR drops significantly at the PA+573 K@Exposure(200 h) state. However, the ACMZ alloy sustains a much higher WHR at 573 K than AC alloy over a wide range of plastic strains. At the PA+573 K@Exposure(200 h) state, the WHR significantly increases over the PA tensile. The high WHR sustains uniform tensile strain. It is evident that the additions of Mn and Zr can contribute to higher strain hardening capability with 573 K@Exposure(200 h) treatment. Meanwhile, premature fractures occur in both alloys by the loss of work hardening ability at higher strain.

Figure 8 shows the representative tensile fracture micrographs for both alloys at the PA state and the PA+573 K@Exposure(200 h) state at 573 K. There are many dimples with different size shapes in both fracture surfaces, which is an indication of the prevalence for ductile fracture. As a result, both alloys have good elongation. The AC alloy is mainly composed of deep and large dimples as a result of severe softening and precipitate coarsening. Comparably, ACMZ alloy is mainly composed of dense and small dimples, suggesting that the HT softening phenomenon rarely occurs in ACMZ alloy.

4 Discussion

In the foregoing section, there are various experimental results of both AC and ACMZ alloys. Herein, we should discuss our experimental observations with respect to (1) the effect of alloy elements Mn and Zr on precipitate evolution during the thermal exposure process, and (2) strengthening mechanisms and ductility behavior during the HT tensile test.

4.1 Precipitate evolution process

A systematic microstructural study has revealed that there are some differences in the HT
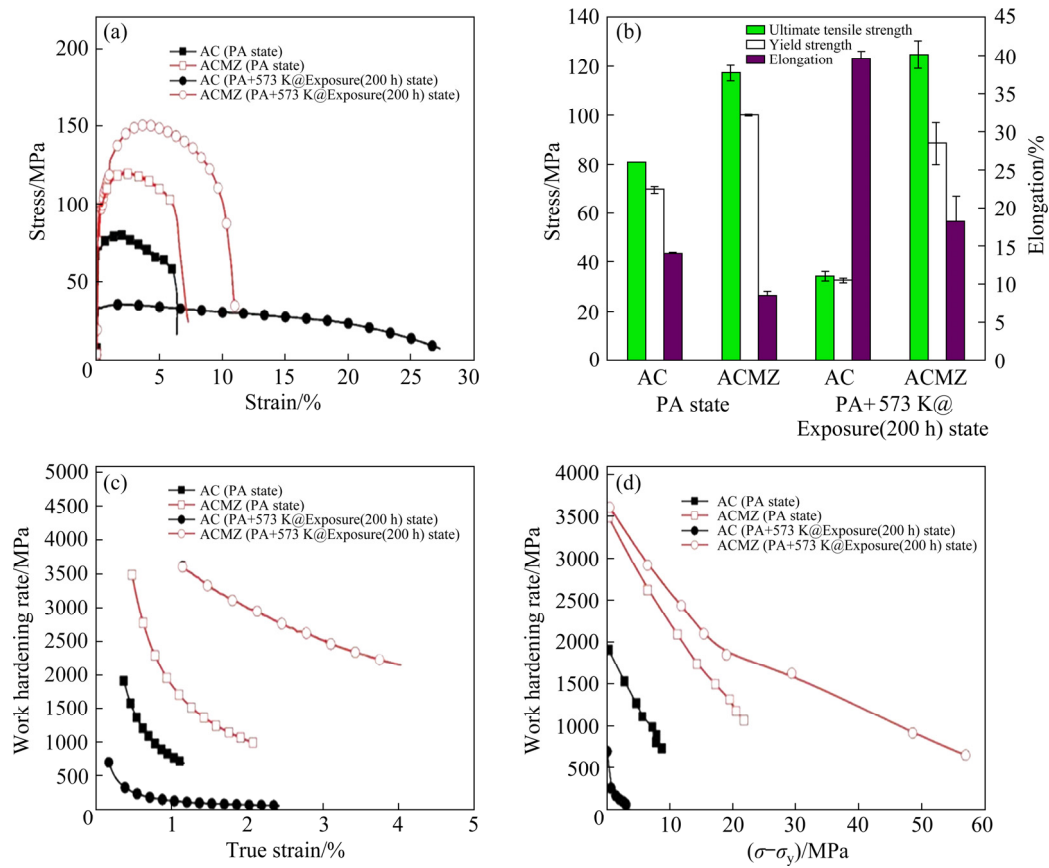
Fig. 7 Tensile stress−strain curves for samples at 573 K with and without 573 K@Exposure(200 h) treatment (a), UTS, YS and EL for AC and ACMZ alloys (b), work hardening rate versus true strain curves (c) and work hardening rate versus $\sigma-\sigma_y$ curves (d)
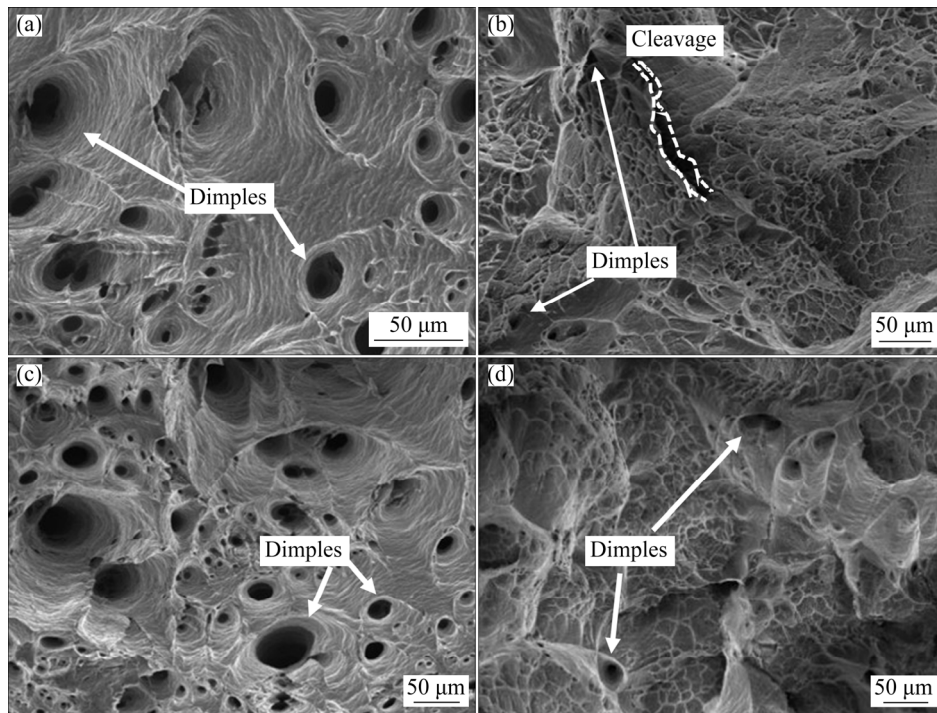

Fig. 8 Representative tensile fractured morphologies at 573 K for AC (a, c) and ACMZ (b, d) alloys: (a, b) PA state; (c, d) PA+573 K@Exposure(200 h) state

mechanical properties of AC and ACMZ alloys. Figure 9 demonstrates the precipitates evolution process characterized by TEM for both as-PAed alloys at 573 K@Exposure(200 h) and 623 K@

Exposure(200 h) states.

For the as-PAed AC alloy (Fig. 9(a)), the homogeneously distributed disk-shaped precipitates (Length: 30.1 nm, Fig. 9(d)) are fine-dispersed
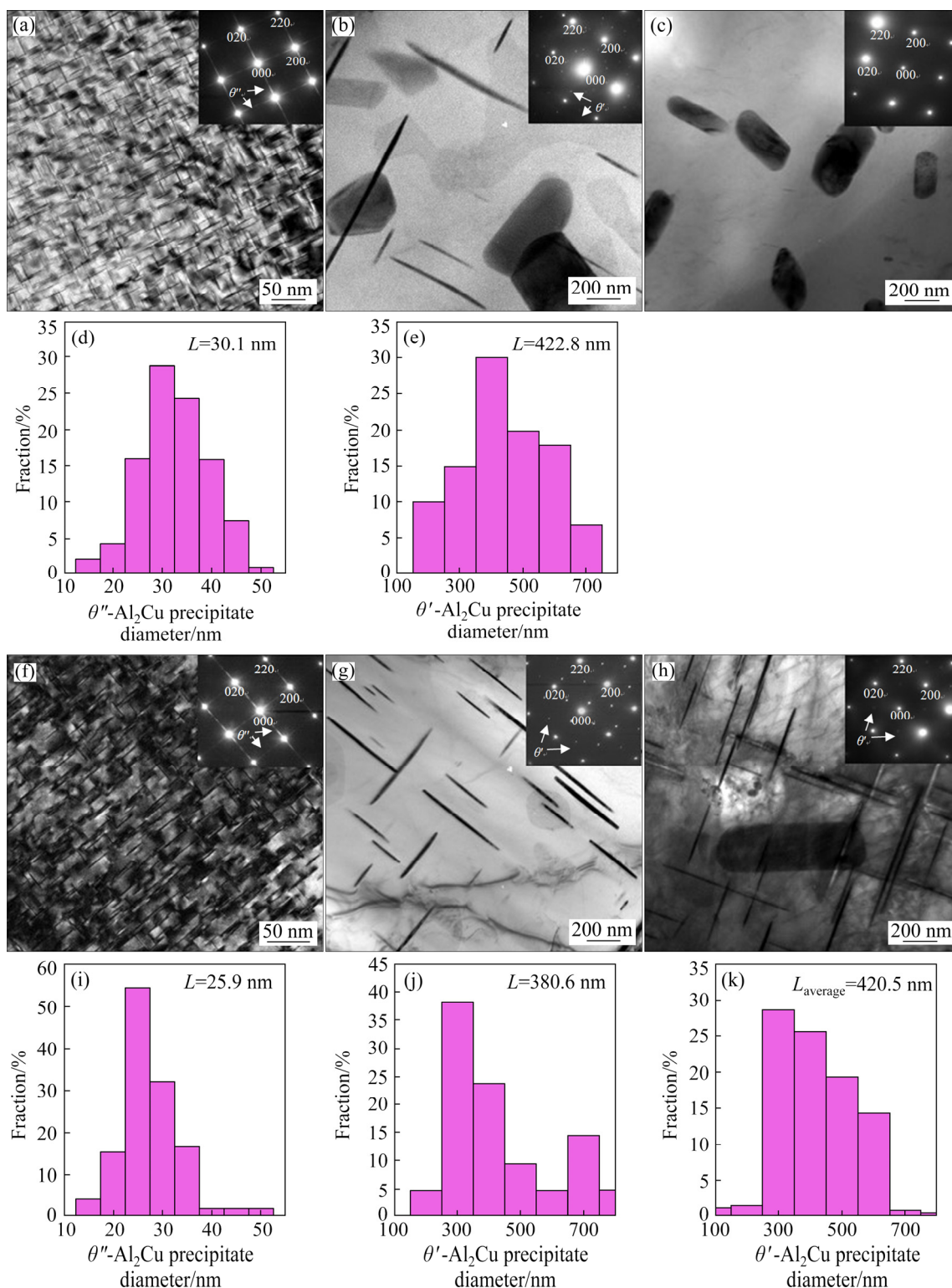
Fig. 9 Comparison of microstructures of AC (a−c) and ACMZ (f−h) alloys with HT microstructure stability and size distributions of θ' and θ'' precipitates in AC (d, e) and ACMZ (i−k) alloys: (a, f) As-PAed state; (b, g) 573 K@Exposure-(200 h) state; (c, h) 623 K@Exposure(200 h) state (TEM images were taken in ⟨001⟩ zone axis for the matrix. The corresponding length size distribution histograms of the θ'' and θ' plates were placed below the images, respectively)

inside Al grains. The selected area electron diffraction (SAED) pattern for the smaller θ'' precipitates embedding in the α(Al) matrix has been confirmed by discontinuous streaks in the pattern [21]. Comparably, the as-PAed ACMZ alloy (Fig. 9(f)) has exhibited a similar microstructure for the precipitates with the as-PAed AC alloy.

At 573 K@Exposure(200 h) state, both larger θ' precipitates (Length: 422.8 nm, Fig. 9(e)) and coarser θ particles are observed in the AC alloy (Fig. 9(b)). Notably, the θ particles have exhibited a near-spherical shape of 440 nm. In the ACMZ alloy (Fig. 9(g)), there are almost all θ' precipitates (Length: 380.6 nm, Fig. 9(j)). In comparison, according to the thermal exposure test results, the hardness of the ACMZ alloy is ~95 HV, which is ~20 HV higher than the AC alloy (~75 HV). It is consistent with the TEM analysis because the θ particles have inferior strengthening effects on Al−Cu alloy [22].

At 623 K@Exposure(200 h) state, the coarser θ particles (~560 nm) are the only precipitates in the AC alloy (Fig. 9(c)), indicating the loss of their strengthening effects to a larger extent. However, there are still mainly θ' precipitates (Length: 420.5 nm, Fig. 9(k)) with few coarse θ particles in the ACMZ alloy (Fig. 9(h)). In comparison, the hardness of AC alloy is only ~47 HV due to the completed appearance of coarser θ particles. ACMZ alloy shows a much higher hardness of ~81 HV, which is almost twice as large as that of AC alloy, due to the huge microstructure difference between both alloys.

The hardness variation with the thermal exposure duration of ACMZ alloy was further tested at 673 K@Exposure(0−200 h). In Fig. 10, the curve shows a two-stage hardness reduction behavior with the finally stabilized hardness of ~57 HV. This value is higher than ~47 HV for AC at 623 K@Exposure(200 h) state, but lower than ~63 HV for the as-cast ACMZ alloy. It is reasonable to assume that at 673 K@Exposure (200 h) state, the precipitation strengthening effect is completely lost and the precipitates are completely transformed into coarser θ particles according to the previous TEM analysis. As a result, the ACMZ alloy has better HT application potential at 673 K, which is ~72% of the absolute melting point of Al, and far above the maximum usage temperature of typical commercial Al alloys.
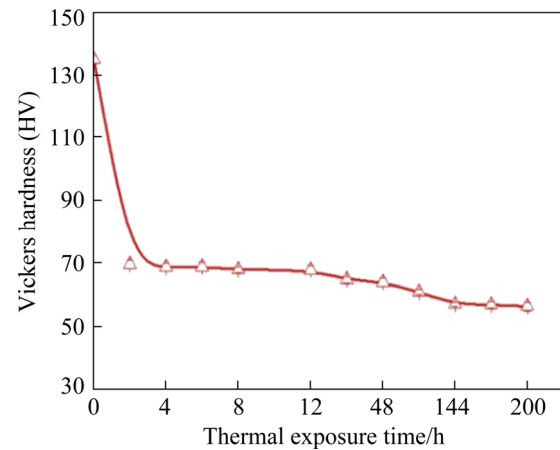

Fig. 10 Hardness values for as-PAed ACMZ alloy at 673 K@Exposure(0−200 h) state

Inspection of the present experimental data shows that precipitation sequences in both AC and ACMZ alloys during the thermal exposure test from RT to 623 K. The following precipitation process occurs: $\theta''\rightarrow\theta'\rightarrow\theta$.

With the prolongation of the thermal exposure duration, the θ'' phases gradually coarsen, and the growth of these phases should consume more solute atoms. When the solute atoms dissolved in the matrix near the GBs are exhausted, the solute atoms can only be replenished by re-dissolving the θ'' phases near the GBs [23]. With the continuous growth of θ'' phases, the metastable phases near GBs gradually dissolve. The θ' precipitate can maintain a semi-coherent relationship with the Al matrix. Once θ' is formed, it may be coarsened to the larger size allowing the bypass of the dislocation line. The semi-coherent relationship is quickly destroyed, and the θ phase is formed. With prolonging exposure time, the formation of the θ phase further accelerates the coarsening process, because the θ phase has high-energy and incoherent interfaces with the Al matrix [24,25]. The θ phase may coarsen at the expense of finer θ' particles, and the mechanical properties of the alloy should deteriorate substantially following this phase transformation (~60% reduction in strength and hardness) [26−29].

Generally, the most significant difference between both alloys is the nature of the θ and θ' precipitates at HTs. In the AC alloy, the morphology, distribution, and dimensions of the strengthening precipitates become less consistent with increasing the temperature. Cu is absorbed from θ' precipitates

by coarsening θ particles which can lead to the rapid growth of blocky particles at the expense of finely dispersed θ' precipitates [26,30]. This means that the strengthening effect of θ particles decreases and the number of available Cu atoms for the more effective θ' precipitate phase decreases. In contrast, the precipitates in the ACMZ alloy retain their coherent and semi-coherent interfaces with the matrix up to 623 K.

Therefore, it is desirable to develop alloys in which the onset of θ' to θ transformation is delayed or prevented at HTs. Such HT stabilization of θ' precipitates has been recently reported to find that the additions of Mn and Zr to an Al−Cu alloy can result in a θ' strengthened microstructure which is morphologically stable at least 623 K [29]. These findings appear to agree with results in Ref. [28], in which mechanisms were proposed to explain the thermal stability of ACMZ alloys. However, the extent of the individual mechanism accounted for the HT microstructural stability in the alloy remains unclear. It is also reported that Mn and Zr atoms tend to segregate to the interfaces between θ' and the Al matrix. This suggests that Mn and/or Zr might reduce the interfacial energy of θ', which can lower the thermodynamic driving force for the precipitate coarsening [30]. Probably, Mn and/or Zr atoms can provide a kinetic barrier, inhibiting the diffusion of Cu atoms from θ' particles [31,32].

The interfacial segregation of Zr and Mn elements retards and potentially stops coarsening by decreasing the interfacial energy (a thermodynamic effect) and creating a diffusion barrier, solute drag, and ledge poison (kinetic effects) [33−35]. The thermodynamically driven coarsening of precipitates explained by the minimization of the total interfacial area can be qualitatively modeled for a binary alloy system by the LSW relationship as mentioned above.

The LSW relationship can be written as [36]

$$\bar{r}^3 - \bar{r}_0^3 = \frac{8}{9}\frac{\gamma D c_0 V_m^2}{RT}(t) \tag{1}$$

where $\bar{r}$ is the θ' equivalent radius at given time t, $\bar{r}_0$ is the starting θ' equivalent radius i.e., in the as-aged state, γ is the interfacial energy, D is the diffusivity of Cu in Al at temperature T, c_0 is the equilibrium concentration of Cu in Al at T, V_m is the molar volume of the precipitate, and R is the molar gas constant.

It can be said that the thermodynamic effect of lower interfacial energy upon segregation helps to reduce the coarsening rate. A corollary that can be drawn to this argument is that kinetic effects are necessary to inhibit coarsening, as observed experimentally. This argument agrees well with the investigations of SHOWER et al [23], where the phase-field simulations suggested synergistic thermodynamic and kinetic effects in retarding the coarsening of θ' precipitates. The exact nature of the kinetic barrier to coarsening is not fully understood for ACMZ alloy microstructure, but may be related to solute drag and ledge poison mechanisms as suggested by POPLAWSKY et al [34].

4.2 Effects of dislocation−precipitation interaction on mechanical properties

4.2.1 Strengthening increment

AC and ACMZ alloys mainly contain θ'' precipitates after the solution and peak-aging treatment in this study. θ'' precipitates are fully coherent with the Al, with atomic layers of Cu replacing Al planes. Al layer is separated by three atomic layers in the normal direction. Coherent θ'' precipitates follow shearing mechanism, whereas θ' is bypassed by Orowan looping [37].

The RT strengthening mechanism of Al−Cu alloys is mainly composed of solid solution strengthening, grain size strengthening, second phase particle strengthening, and dislocation strengthening. The overall YS ($\sigma_{0.2}$) of Al−Cu alloys can be expressed as

$$\sigma_{0.2} = \sigma_0' + \sigma_{ss} + \sigma_{gs} + \sigma_{or} \tag{2}$$

where σ_0' is the yield strength of pure Al (taken as 35 MPa [37]), σ_{ss} is the solid solution strength, σ_{gs} is the grain size strengthening, and σ_{or} is the Orowan strengthening, which consists of the second phase particle strengthening and dislocation strengthening.

The solid solution strengthening from Cu in the Al matrix is 7 MPa per mass percent [38]. Therefore, the YS increases because the solid solution strengthening in both alloys is similar while there exists slight difference in the content of solute elements.

Grain size strengthening is calculated using the Hall−Petch equation:

$$\sigma_{gs} = \sigma_i + K d^{-1/2} \tag{3}$$

where σ_i is the YS of Al alloys (taken as 29 MPa [33]), K is a constant related to materials (taken as 0.08 MPa·m$^{1/2}$ [37]), and d is the average grain size of the materials.

The average grain size of AC alloy at the as-PAed states is ~250 μm. For ACMZ alloy, it is ~223 μm. Therefore, it has been inferred that the similar values of these grain sizes should possess similar levels of possible grain size strengthening.

The θ'' phases consist of ordered groups of solute atoms and possess lower vacancy concentration and stronger internal stress field [39]. A large amount of finely dispersed θ'' in AC and ACMZ alloys can hinder the dislocation line movement, so both alloys show good mechanical properties at RT.

In general, the deformation resistance of metals decreases with the elevated temperature. At HTs, the cross-slip and climb of dislocations become easier, and the bonding force between atoms is further weakened, which leads to the HT softening [40]. CALALIERE and MARCO [41] and EMAMI et al [42] showed that the intermetallic phases with HT stability had a strong pining effect on GBs and sub-GBs during the deformation of Al alloys at HTs, which can compensate for the GB weakening at HTs.

At the 573 K@Exposure(200 h) state, the phase transformation occurs and the main composition phase is θ' for ACMZ alloy. θ' is the primary strengthening precipitate in Al−Cu-based alloy. Hence, the tensile strength of ACMZ alloy at the PA+573 K@Exposure(200 h) state is higher than that of the as-PAed alloy. In AC alloy, the phase transformation occurs after 573K @Exposure (200 h) treatment, and θ' transforms to θ herein. The coarse θ phase should rarely contribute to the strengthening effect, but can be severely detrimental to ductility and especially fracture toughness of the Al−Cu alloys as the void/crack initiators of the preferential crack paths.

In Al−Cu-based alloys, the HT stability of the θ' precipitates (i.e., the size and quantity of the θ' precipitates at HTs) has an important influence on their HT strengthening effect. The influence of the volume fraction, number density, size, and other factors of the spherical shear-resistant precipitate on the strength of the material can be expressed by the traditional Orowan formula [43]. Clearly, either increasing the volume fraction/number density or

reducing the size of the spherical precipitate can effectively increase the strength of the material. However, the θ' precipitate is a disc-shaped particle with a large diameter-to-thickness ratio, and cannot be approximated as a spherical shape. Therefore, the traditional Orowan formula cannot be used to express the relationship between θ' precipitate and strength. Recently, some researchers have proposed a strengthening model suitable for the disc-shaped θ' precipitates in Al−Cu alloys by modifying the Orowan formula [33]. For example, NIE and MUDDLE [44] proposed the relationship between the size, volume fraction, number density and other factors of the θ' precipitate and the YS ($\sigma_{\theta'}$). The formula is as follows:

$$\sigma_{or} = \sigma_{\theta'} = \frac{MGb}{2\pi\sqrt{1-\upsilon}} \cdot$$
$$\left\{ 1 \Big/ \left[\left(\frac{3.247}{fAN_V^2}\right)^{\frac{1}{6}} - \left(\frac{0.077fA}{N_V}\right)^{\frac{1}{3}} - \left(\frac{1.521f}{N_V A^2}\right)^{\frac{1}{3}} \right] \right\} \cdot$$
$$\ln\left\{ \frac{1.063}{b}\left(\frac{f}{N_V\sqrt{A}}\right)^{\frac{1}{3}} \right\} \qquad (4)$$

where M is the Taylor factor, G is the shear modulus of Al, υ is the Poisson's ratio of Al, b is the Burgers vector component of Al, A is the diameter-to-thickness ratio of the θ' precipitate (diameter d and thickness t), f is the volume fraction of θ' precipitate, and N_V is the number density of θ' precipitate.

Through the analysis of this strengthening model, it can be concluded that when the volume fraction of the precipitated phase of θ' remains unchanged, the smaller the diameter of the θ' precipitate is, the greater the number density is, which can lead to more significant increase in strength [45]. Compared with AC alloy, ACMZ alloy owns more θ' precipitates with smaller sizes, which have more significant precipitation strengthening effect.

4.2.2 Ductility

The typical Considère criterion is usually used to predict plastic instability (the necking point) [46]. This criterion indicates that a higher WHR can suppress the necking point, which leads to a higher ductility referring to the uniform elongation [47]. Herein, the uniform strain describes global deformation before the necking of the alloy under

uniaxial tension. From the microstructure characterization of all alloys (the average grain size is very similar), the difference between the WHRs of AC and ACMZ alloys at the PA and PA+573 K@ Exposure(200 h) states is mainly dominated by the precipitates [48]. It is well known that the interaction between the precipitates and dislocations is the dislocation bypassing mechanism during deformation for Al−Cu-based alloys. On the one hand, the precipitates can hinder the dislocation motion, leading to the dislocation pile-up [49]. On the other hand, the accumulated dislocation density in terms of Orowan loops can promote a higher WHR during deformation according to previous results [50,51].

ACMZ alloy has the highest WHR, which is due to its higher density of precipitates (θ'). The significantly high ductility of ACMZ alloy is caused by two microstructural changes occurring during 573 K thermal exposure: the dramatic decrease in dislocation density, and the precipitation of a high density of nano-sized θ' phase precipitates. The extremely low dislocation density after thermal exposure leaves much room for dislocation accumulation, which should certainly increase the WHR [52]. The high density of nano-θ' phase precipitates provides effective sites for trapping and accumulation dislocations, which should also increase the WHR [53]. Therefore, it is reasonable to infer that the dislocation increases faster during deformation and stores a higher density of dislocation density for the ACMZ alloy at PA + 573 K@Exposure(200 h) state compared with the AC alloy. It is the faster increase in dislocation density and the higher storage dislocation density in the ACMZ alloy, which should result in a higher WHR and lead to a higher ductility finally.

5 Conclusions

(1) Al−5%Cu (AC) and Al−5%Cu−0.2%Mn−0.2Zr% (ACMZ) alloys exhibit obvious age-hardening behavior during aging treatment. AC alloy reaches the PA state at 4 h and obvious softening behavior from 18 to 28 h, when the hardness decreases at 0.5 HV/h. In comparison, the ACMZ alloy also takes 4 h to reach the PA state but has no obvious hardness reduction from 4 to 28 h.

(2) Mn and/or Zr might reduce the interfacial energy of θ', which lowers the thermodynamic driving force for particle coarsening. The θ' precipitates in the ACMZ alloy remained thermally stable during thermal exposure at 623 K@ Exposure(200 h) state, and the precipitates of AC alloys were mostly θ particles that underwent coarsening. Micro-alloying with Mn and Zr elements remarkably improved HT microstructure stability of Al−Cu alloy.

(3) The ACMZ alloy had a high tensile strength of (88.6±8.8) MPa, good elongation of (18.3±3.3)%, and high hardness of 95 HV at PA+573 K@Exposure(200 h) state, which were higher than those of the AC alloy. The increased HT strength was mainly attributed to the precipitate strengthening and dislocation strengthening, and the enhanced ductility was because the θ' precipitates hindered the dislocation motion and promoted work hardening rate.

Acknowledgments

References

[1] JAVIDANI M, LAROUCHE D. Application of cast Al−Si alloys in internal combustion engine components [J]. International Materials Reviews, 2014, 59: 132−158.

[2] ROY S, ALLARD L F, RODRIGUEZ A, WATKINS T R, SHYAM A. Comparative evaluation of cast aluminum alloys for automotive cylinder heads: Part Ⅰ — Microstructure evolution [J]. Metallurgical and Materials Transactions A, 2017, 48: 2529−2542.

[3] ZHANG Jia-ying, ZUO Li-jie, FENG Jian, YE Bing, KONG Xiang-yang, JIANG Hai-yan, DING Wen-jiang. Effect of thermal exposure on microstructure and mechanical properties of Al−Si−Cu−Ni−Mg alloy produced by different casting technologies [J]. Transactions of Nonferrous Metals Society of China, 2020, 30: 1717−1730.

[4] LIAO Heng-cheng, XU He-ting, HU Yi-yun. Effect of RE addition on solidification process and high-temperature strength of Al−12%Si−4%Cu−1.6%Mn heat-resistant alloy [J]. Transactions of Nonferrous Metals Society of China, 2019, 29: 1117−1126.

[5] WANG An, WANG Hong-ze, WU Yi, WANG Hao-wei. 3D

printing of aluminum alloys using laser powder deposition: A review [J]. The International Journal of Advanced Manufacturing Technology, 2021, 116: 1−37.

[6] LI Yao, XU Guo-fu, PENG Xiao-yan, LIU Shi-chao, DOU Yu-hai, LIANG Xiao-peng. High temperature mechanical properties and microstructure of die forged Al−5.87Zn−2.07Mg−2.42Cu alloy [J]. Transactions of Nonferrous Metals Society of China, 2020, 30: 1771−1779.

[7] DING Li-peng, JIA Zhi-hong, NIE Jian-feng, WENG Yao-yao, CAO Ling-fei, CHEN Hou-wen, WU Xiao-zhi, LIU Qing. The structural and compositional evolution of precipitates in Al−Mg−Si−Cu alloy [J]. Acta Materialia, 2018, 145: 437−450.

[8] LIN Y C, XIA Yu-chi, MA Xue-song, JIANG Yu-qiang, CHEN Ming-song. High-temperature creep behavior of Al−Cu−Mg alloy [J]. Materials Science and Engineering A, 2012, 550: 125−130.

[9] ZHU L, LI N, CHILDS P R N. Light-weighting in aerospace component and system design [J]. Propulsion and Power Research, 2018, 7: 103−119.

[10] SHAHA S K, CAERWINSKI F, KASPRZAK W, FRIEDMAN J, CHEN D L. Monotonic and cyclic deformation behavior of the Al−Si−Cu−Mg cast alloy with micro-additions of Ti, V and Zr [J]. International Journal of Fatigue, 2015, 70: 383−394.

[11] JIA Hao-lin, WANG Hong-ze, WU Yi, WANG Hao-wei. Scanning-strategy in selective laser melting (SLM): A review [J]. The International Journal of Advanced Manufacturing Technology, 2021, 113: 2413−2435.

[12] GUINIER A. Heterogeneities in solid solutions [J]. Solid State Physics, 1959, 9: 293−398.

[13] CVIJOVIĆ Z, RADENKOVIĆ G, MAKSIMOVIĆ V, DIMČIĆ B. Application of ANOVA method to precipitation behaviour studies [J]. Materials Science and Engineering A, 2005, 397: 195−203.

[14] ABDI M, SHABESTARI S G. Novel high strength Al−10.5Si−3.4Cu−0.2Mg alloy produced through two-stage solution heat treatment [J]. Transactions of Nonferrous Metals Society of China, 2021, 31: 576−585.

[15] LU Jiang, BAPTISTE R, TIMOTHY L, THOMAS D. Coupled segregation mechanisms of Sc, Zr and Mn at θ' interfaces enhances the strength and thermal stability of Al−Cu alloys [J]. Acta Materialia, 2021, 206: 116634.

[16] HE Yi, XI Hai-hui, MING Wen-quan, SHAO Qin-qin, SHEN Ruo-han, LAI Yu-xiang, WU Cui-lan, CHEN Jiang-hua. Thermal stability and precipitate microstructures of Al−Si−Mg−Er alloy [J]. Transactions of Nonferrous Metals Society of China, 2021, 31: 1−10.

[17] POZDNIAKOV A V, BARKOV R Y. Microstructure and materials characterisation of the novel Al−Cu−Y alloy [J]. Materials Science and Technology, 2018, 34: 1489−1496.

[18] SHIN D, SHYAM A, LEE S, YAMAMOTO Y, HAYNES J A. Solute segregation at the Al/θ'-Al$_2$Cu interface in Al−Cu alloys [J]. Acta Materialia, 2017, 141: 327−340.

[19] SHYAM A, ROY S, SHIN D, POPLAWSKY J D, ALLARD L F, YAMAMOTO Y, MORRIS J R, MAZUMDER B, IDROBO J C, RODRIGUEZ A, WATKINS T R, HAYNES J A. Elevated temperature microstructural stability in cast AlCuMnZr alloys through solute segregation [J]. Materials

[20] CHEN T, JIANG Z X, PENG H, HE H L, WANG L L, WANG Y G. Effect of grain size on the spall fracture behaviour of pure copper under plate-impact loading [J]. Strain, 2015, 51: 190−197.

[21] MAJINENI S K, SUGATHAN S, MEHER S, BANERJEE R, BHATTACHARYA S, KUMAR S, CHATTOPADHYAY K. Enhancing elevated temperature strength of copper containing aluminium alloys by forming L1$_2$ Al$_3$Zr precipitates and nucleating θ'' precipitates on them [J]. Scientific Reports, 2017, 7: 11154.

[22] LUMLEY R N, MORTON A J, POLMEAR I J. Enhanced creep performance in an Al−Cu−Mg−Ag alloy through underaging [J]. Acta Materialia, 2002, 50: 3597−3608.

[23] SHOWER P, MORRIS J, SHIN D, RADHAKRISHNAN B, POPLAWWSKY J, SHYAM A. Mechanisms for stabilizing θ'(Al$_2$Cu) precipitates at elevated temperatures investigated with phase field modeling [J]. Materialia, 2019, 6: 100335.

[24] NIE J F, MUDDLE B C. Microstructural design of high-strength aluminum alloys [J]. Journal of Phase Equilibria, 1998, 19: 543−551.

[25] KOKOTIN V, HECHT U. Molecular dynamics simulations of Al−Al$_2$Cu phase boundaries [J]. Computational Materials Science, 2014, 86: 30−37.

[26] MILLIGAN B K, ROY S, HAWKINS C S, ALLARD L F, SHYAM A. Impact of microstructural stability on the creep behavior of cast Al−Cu alloys [J]. Materials Science and Engineering A, 2019, 772: 138697.

[27] SHOWER P, ROY S, HAWKINS C S, SHYAM A. The effects of microstructural stability on the compressive response of two cast aluminum alloys up to 300 °C [J]. Materials Science and Engineering A, 2017, 700: 519−529.

[28] ROY S, ALLARD L F, RODRIGUEZ A, PORTER W D, SHYAM A. Comparative evaluation of cast aluminum alloys for automotive cylinder heads: Part II—Mechanical and thermal properties [J]. Metallurgical and Materials Transactions A, 2017, 48: 2543−2562.

[29] ALLOYS A. Aluminum and aluminum alloys [M]. New Jersey: John Wiley and Sons Inc, 2006.

[30] PORTER D, EASTERRLING K. Phase transformations in metals and alloys [M]. Boca Raton: Van Nostrand Reinhold, 1992.

[31] MONACHON C, KRUG M E, SEIDMAN D N, DUNAND D C. Chemistry and structure of core/double-shell nanoscale precipitates in Al−6.5Li−0.07Sc−0.02Yb (at.%) [J]. Acta Materialia, 2011, 59: 3398−3409.

[32] SANKARAN R, LAIRD C. Kinetics of growth of platelike precipitates [J]. Acta Metallurgica, 1974, 22: 957−969.

[33] ZHU A W, STARKE E A Jr. Strengthening effect of unshearable particles of finite size: A computer experimental study [J]. Acta Materialia, 1999, 47: 3263−3269.

[34] POPLAWSKY J D, MILLIGAN B K, ALLARD L F, SHIN D W, SHOWER P, CHISHOLM M F, SHYAM A. The synergistic of Mn and Zr/Ti in producing θ'/L12 co-precipitates in Al−Cu alloys [J]. Acta Materialia, 2020, 194: 577−586.

[35] FINE M E, BURELL D L, ELIEZER Z, PERSAD C, MARCUS H L. Basic principles for selecting phases for high

temperature metal matrix composites: Interfacial considerations [J]. Scripta Metallurgica, 1988, 22(6): 907−910.

[36] BOYD J D, NICHOLSON R B. The coarsening behavior of θ'' and θ' precipitates in two Al−Cu alloys [J]. Acta Metallurgica, 1971, 19(12): 1379−1391.

[37] SHANMUGASUNDARAM T, HEILMAIER M, MURTY B S, SARMA V S. On the Hall−Petch relationship in a nanostructured Al−Cu alloy [J]. Materials Science and Engineering A, 2010, 527: 7821−7825.

[38] BAUCCIO M. ASM metals reference book [M]. New York: ASM International, 1993.

[39] GUPTA A K, LLOYD D J, COURT S A. Precipitation hardening in Al−Mg−Si alloys with and without excess Si [J]. Materials Science and Engineering A, 2001, 316: 11−17.

[40] HERNANDEZ-SANDOVAL J, GARZA-ELIZONDO G H, SAMUEL A M, VALTIIERRA S, SAMUEL F H. The ambient and high temperature deformation behavior of Al−Si−Cu−Mg alloy with minor Ti, Zr, Ni additions [J]. Materials and Design, 2014, 58: 89−101.

[41] CAVALIERE P, MARCO P P D. Friction stir processing of a Zr-modified 2014 aluminium alloy [J]. Materials Science and Engineering A, 2007, 462: 206−210.

[42] EMAMI A R, BEGUM S, CHEN D L, SKSZEK T, NIU X P, ZHANG Y, GABBIANELLI F. Cyclic deformation behavior of a cast aluminum alloy [J]. Materials Science and Engineering A, 2009, 516: 31−41.

[43] TEIXEIRA J D, CRAM D G, BOURGEOIS L, BASTOW T J, HILL A J, HUTCHINSON C R. On the strengthening response of aluminum alloys containing shear-resistant plate-shaped precipitates [J]. Acta Materialia, 2008, 56: 6109−6122.

[44] NIE J F, MUDDLE B C. Strengthening of an Al−Cu−Sn alloy by deformation-resistant precipitate plates [J]. Acta Materialia, 2008, 56: 3490−3501.

[45] MA P P, LIU C H, WU C L, LIU L M, CHEN J H. Mechanical properties enhanced by deformation-modified precipitation of θ'-phase approximants in an Al−Cu alloy [J]. Materials Science and Engineering A, 2016, 676: 138−145.

[46] CONSIDÈRE A. Mémoire sur l'emploi du fer et de l'acier dans les constructions [J]. Annales des Ponts et Chaussées, 1885, 9: 574−605.

[47] YANIKOV I S, VINOGRADOV A, ESTRIN Y. Revisting the Considère criterion from the view point of dislocation theory fundamentals [J]. Scripta Materialia, 2014, 76: 37−40.

[48] ESTRIN Y. Unified constitutive laws of plastic deformation [M]. New York: Academic Press Inc, 1996.

[49] GLADMAN T. Precipitation hardening in metals [J]. Materials Science and Technology, 1999, 15(1): 30−36.

[50] ZHAO Y H, LIAO X Z, CHENG S, MA E, ZHU Y T. Simultaneously increasing the ductility and strength of nanostructured alloys [J]. Advanced Materials, 2006, 18: 2280−2283.

[51] WANG Y M, MA E. Three strategies to achieve uniform tensile deformation in a nanostructured metal [J]. Acta Materialia, 2004, 52(6): 1699−1709.

[52] HUTCHINSON B, RIDLEY N. On dislocation accumulation and work hardening in Hadfield steel [J]. Scripta Materialia, 2006, 55(4): 299−302.

[53] CHENG S, ZHAO Y H, ZHU Y T, MA E. Optimizing the strength and ductility of fine structured 2024 Al alloy by nano-precipitation [J]. Acta Materilia, 2007, 55: 5822−5832.

Zr 和 Mn 元素微合金化增强耐高温铝铜合金的热稳定性和力学性能

孙腾腾 [1,2]，耿继伟 [1,2]，卞泽宇 [1,2]，吴一 [1,2]，汪明亮 [1]，陈 东 [2,3]，马乃恒 [2]，王浩伟 [1,2]

1. 上海交通大学 材料科学与工程学院，上海 200240；
2. 上海交通大学 金属基复合材料国家重点实验室，上海 200240；
3. 安徽省铝基复合材料工程研究中心，淮北 235099

摘 要：系统研究 Al−5%Cu (AC)和 Al−5%Cu−0.2%Mn−0.2Zr% (ACMZ)合金在温度为 573~673 K 的高温热稳定性和力学性能。结果表明，微合金化添加 Zr 和 Mn 元素对 573 K 主要强化相 θ'相的稳定起到至关重要的作用。同时，高温拉伸结果表明，573 K 热暴露 200 h 后，ACMZ 合金强度为(88.6±8.8) MPa，远高于相同状态下 AC 合金的强度((32.5±0.8) MPa)。最后，讨论高温状态下 ACMZ 合金的强度和塑性强化机制。

关键词：铝铜合金；微合金化；热稳定性；析出相演变；高温力学性能

(Edited by Wei-ping CHEN)